Evolution of Quasicrystals and Long-Period Stacking Ordered Structures During Severe Plastic Deformation and Mixing of Dissimilar Mg Alloys Upon Friction Stir Welding

Meichen Liang[1] · Hao Zhang[1] · Lifeng Zhang[1] · Peng Xue[1] · Dingrui Ni[1] · Weizhen Wang[1] · Zongyi Ma[1] · Hengqiang Ye[1,2] · Zhiqing Yang[1]

Abstract

Microstructural evolution during severe plastic deformation and mixing of $Mg_{95.8}Zn_{3.6}Gd_{0.6}$ and $Mg_{97}Cu_1Y_2$ (at%) alloys upon friction stir welding was studied. A laminated onion-ring structure composed of alternative distribution of layers with significantly refined microstructures from different alloys was formed in the stirred zone. Coarse quasicrystals were broken up and dispersed with most of them being transformed into cubic W-phase particles, and thick 18R long-period stacking ordered plates were fractured and transformed into fine 14H-LPSO lamellae in the stirred zone (SZ) experiencing complex material flow under high strain rate. Fine W-phase particles and 14H-LPSO lamellae formed during dissimilar friction stir welding (FSW) usually have no specific orientation relationship with surrounding Mg matrix. Chemical measurements demonstrated occurrence of interdiffusion between dissimilar layers in the SZ. Phase transformation was observed for some particles of quasicrystals and long-period stacking ordered (LPSO) in regions slightly outside the SZ. An ultimate tensile strength of ~415 MPa and an elongation to failure of ~27.8%, both exceeding those of base materials, were obtained in the SZ, due to microstructural refinement and formation of a laminated structure.

Keywords Mg alloy · Microstructure · Phase transformation · Severe plastic deformation · Mechanical property

1 Introduction

Mg alloys present low density and high specific strength and have great potentials for various applications [1–4]. Mg–TM–RE (TM, transition metal, and RE, rare earth) alloys with icosahedral quasicrystal (IQC) or long-period stacking ordered (LPSO) strengthening phases have received considerable attention, due to their superior mechanical properties at both the ambient and elevated temperatures [5–10]. IQCs and LPSO structures are usually quite coarse and distributed mainly at grain boundaries (GBs) in as-cast Mg alloys; hence, their refinement and dispersion are necessary to achieve better strengthening effects [11, 12]. Severe plastic deformation (SPD) has been employed to effectively refine microstructures of metals and alloys [13–17]. Friction stir welding (FSW)/friction stir processing (FSP) is emerging as a very effective solid-state joining/processing technique, which has been extensively demonstrated in various industries [18–24]. FSW/FSP not only involves complex material flow and mixing under strain rates much higher than other SPD techniques (like high-pressure torsion and equal channel angular pressing [15–17]), but also results in localized heating due to friction between tool and workpieces, both influencing the microstructures of materials [18]. During proper FSW/FSP, the materials thus undergo intense plastic deformation at elevated temperature, producing joints or materials showing good mechanical properties, due to generation of fine microstructures [18].

Hot extrusion or rolling has been exploited widely for microstructural modification of Mg–TM–RE alloys,

especially in terms of refinement of IQC and LPSO phases, to improve their mechanical properties [9–12]. Recently, Mg alloys with IQC or LPSO have been successfully processed or welded by friction stir methods [25–29]. It was reported that the tensile strength of a Mg–Zn–Y–Zr alloy with IQCs was decreased to 95% of that of the base material after FSW [27]. Coarse IQCs in Mg–Zn–Y–Zr alloys were broken up and dispersed with some of them being transformed into W-phase during FSP or FSW [26, 27]. Yang et al. [28, 29] studied the influence of temperature, plastic strain and cooling rate on the distribution of LPSO phase in Mg–Gd–Y–Zn–Zr alloys subjected to friction stir processing (FSP) and successfully developed a microstructure with LPSO lamellae mainly within Mg grains, which simultaneously improved the tensile strength and ductility, from 249 to 380 MPa and from 7.9 to 21.5%. Microstructural evolution involved in SPD with complex material flow, and mixing of dissimilar Mg–TM–RE alloys with IQCs and LPSO structures has not been investigated comprehensively to date, although there have been some studies on SPD of such alloys [17, 26–30].

In the present study, $Mg_{95.8}Zn_{3.6}Gd_{0.6}$ and $Mg_{97}Cu_1Y_2$ (at%) as-cast alloys containing, respectively, IQC and LPSO strengthening phases were treated by FSW. The microstructural evolution was investigated using various electron microscopy techniques, with more efforts focused on evolution of IQCs and LPSO structures in the stirred zone (SZ) which experienced complex material flow and mixing as a result of SPD under high strain rates. The SZ of $Mg_{95.8}Zn_{3.6}Gd_{0.6}/Mg_{97}Cu_1Y_2$ joints showed tensile strength and ductility much better than both basal materials, which is in contrast to the decreased tensile strength or ductility observed in some FSWed or FSPed Mg alloys with IQCs [27] or LPSO phases [25]. The present results may shed light on studies of microstructural modification to improve properties of Mg–TM–RE alloys through SPD techniques like FSW or FSP.

2 Experimental

Two Mg alloys with nominal compositions of, respectively, $Mg_{95.8}Zn_{3.6}Gd_{0.6}$ and $Mg_{97}Cu_1Y_2$ (at%) were produced by high-frequency induction melting under an argon atmosphere. The melt was cast into a steel mold preheated to ~ 573 K. Plates 8 mm thick were machined from as-cast samples. Prior to SPD using FSW, the surfaces were polished to remove oxides and cleaned using ethanol. FSW was carried out with a tool rotation rate of 1500 rpm and a traverse speed of 25 mm min^{-1}, according to previous FSP of Mg–TM–RE alloys [27–29, 31]. A tool of Inconel 718 alloy with a shoulder 18 mm in diameter and a threaded cylindrical pin of 6 mm in diameter and 6 mm in

length was used. $Mg_{95.8}Zn_{3.6}Gd_{0.6}$ and $Mg_{97}Cu_1Y_2$ plates were placed, respectively, at the advancing side (AS) and retreating side (RS) [21, 31], as shown schematically in Fig. 1a, based on results of tensile tests of base materials. The maximum strain rate for the present FSW was estimated to be ~ 75 s^{-1} according to evaluation using a torsion deformation model [32].

In order to understand microstructural evolution accompanying the SPD and complex material flow and mixing during FSW, electron microscopy characterizations of cross sections perpendicular to the welding direction of the joint were performed. Scanning electron microscopy (SEM) investigations were carried out using a FEI/Philips XL30 FEG machine. Grain sizes were evaluated from SEM images using the line intersection method. Transmission electron microscopy (TEM), high-angle annular dark-field scanning transmission electron microscopy (HAADF-STEM), electron diffraction and X-ray energy-dispersive spectroscopy (EDS) studies were performed using a Tecnai F30 microscope and an aberration-corrected Titan 600–300 microscope, both operating at 300 kV. Microhardness of the joint was measured along the mid-thickness line on the cross section using a MH-3 Vickers microhardness tester, as illustrated by a red dashed line schematically in Fig. 1b. A load of 20 g and a dwell time of 10 s were used. Tensile specimens with a gauge length of 2.5 mm, a gage width of 1.4 mm and a gage thickness of 0.8 mm were machined from the joint in the cross section perpendicular to the welding direction, with the gauge being centered in the SZ. Figure 1c illustrates the tensile specimen geometry. Tensile tests were conducted at a strain rate of 1×10^{-3} s^{-1} using an Instron 5848 microtester.
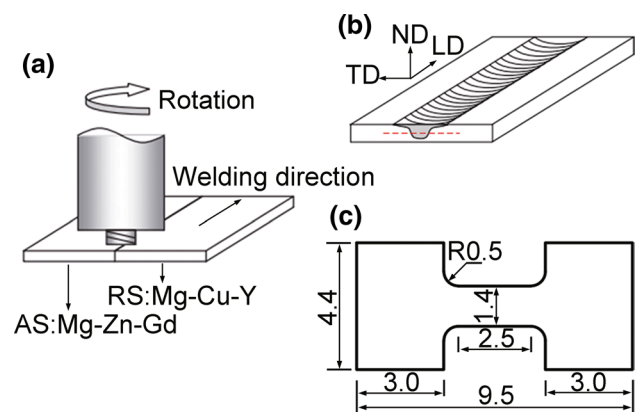

Fig. 1 Schematic illustration of experiments: **a** friction stir welding, **b** Vickers microhardness measurement, **c** geometry and size of tensile specimens in mm

3 Results

Figure 2a shows a typical optical macrograph for the dissimilar joint with a clearly resolved SZ. Figure 2b shows a magnified optical macrograph of the FSW SZ. No apparent defects, such a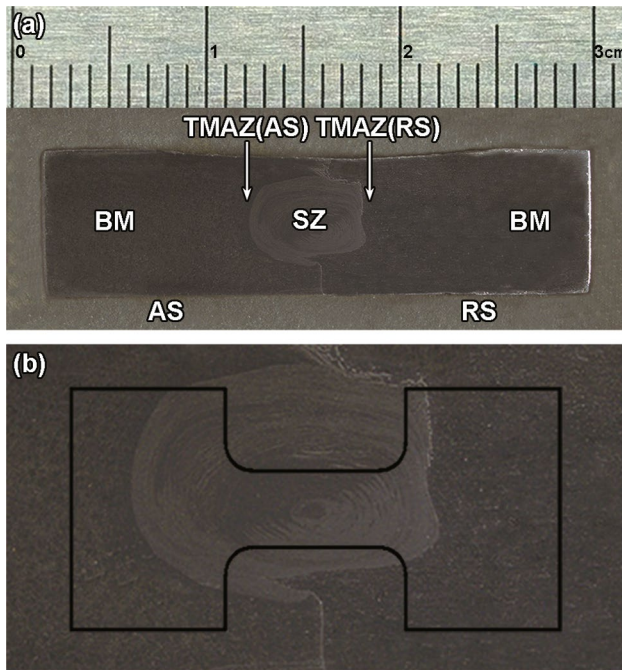s porosity and cracks, were observed on the cross section, indicating that a compact structure was produced as a result of SPD involving complex material flow and mixing during FSW. In FSW joints, several distinct regions can normally be recognized, including SZ, thermo-mechanical-affected zone (TMAZ), heat-affected zone (HAZ) and base materials, due to the difference in plastic deformation and frictional heat [18]. In the present case, all the regions except HAZ were clearly observed in the joint, which was further verified by SEM observations. This phenomenon should be attributed to the low heat input of the FSW in comparison with traditional fusion welding, the excellent heat dissipation ability of Mg alloys [33], as well as the better microstructural thermostability of Mg alloys with RE addition [34].

3.1 Microstructures

3.1.1 Microstructures of As-Cast Alloys

Figure 3a shows a back-scattered electron (BSE) SEM image of the as-cast $Mg_{95.8}Zn_{3.6}Gd_{0.6}$ alloy, showing an average Mg grain size ~ 30 μm. Dendritic secondary phases with bright contrast are mostly distributed at GBs. The inset in Fig. 3a is a selected area electron diffraction (SAED) pattern revealing a fivefold symmetry, demonstrating that secondary phases in the as-cast $Mg_{95.8}Zn_{3.6}Gd_{0.6}$ alloy are IQCs [34]. Figure 3b shows a BSE-SEM image of the as-cast $Mg_{97}Cu_1Y_2$ alloy, showing that the average Mg grain size is ~ 50 μm. There are intensity spots at positions of $n/6$ $(0002)_{Mg}$ (n is an integer) in the SAED pattern for the second phase with bright contrast (inset in Fig. 3b), indicating the presence of 18R-LPSO structures in the as-cast $Mg_{97}Cu_1Y_2$ alloy [8, 35].
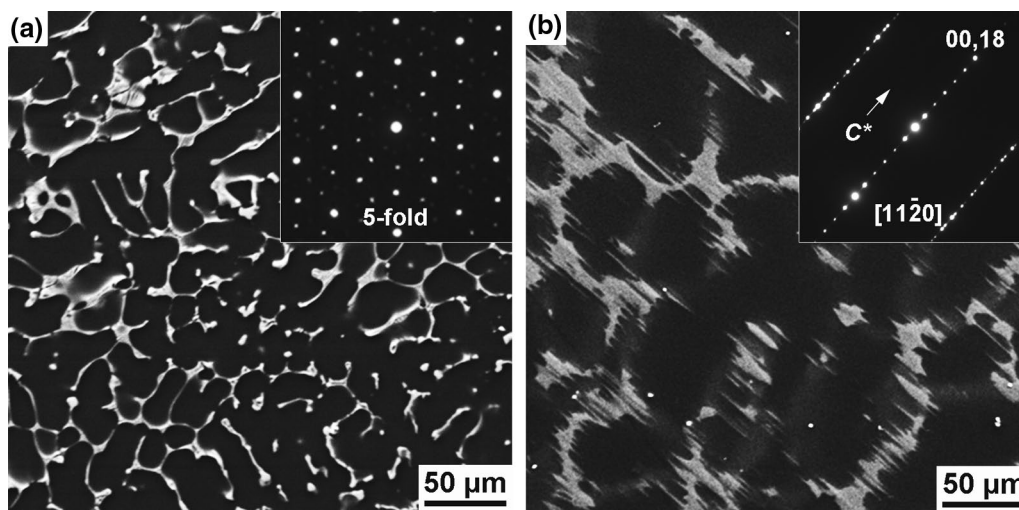

Fig. 2 a Optical macrograph of the $Mg_{95.8}Zn_{3.6}Gd_{0.6}/Mg_{97}Cu_1Y_2$ FSW joint; BM stands for base materials. **b** Magnified optical macrograph of the FSW SZ, showing the position of tensile specimens

Fig. 3 BSE-SEM micrographs for **a** $Mg_{95.8}Zn_{3.6}Gd_{0.6}$, **b** $Mg_{97}Cu_1Y_2$. Insets in **a**, **b** show SAED patterns recorded along the fivefold axis of IQCs and the $[11\bar{2}0]$ zone axis of LPSO plates

3.1.2 Microstructures of TMAZ

Figure 4a, b shows BSE-SEM micrographs for the TMAZ at the AS and RS, respectively. It can be seen clearly that Mg grains in the TMAZ adjacent to the TMAZ/SZ interfaces were elongated along the shear direction, compared with those in base materials far away from the SZ (Fig. 3), demonstrating the occurrence of severe plastic deformation. And deformation of grains decreased with increasing distance from the SZ. No thermally driven grain growth was observed within the TMAZ. Figure 4c, d shows enlarged images for regions indicated by black rectangles in Fig. 4a, b, respectively. It can be seen that widths of Mg bands in the TMAZ adjacent to the TMAZ/SZ interfaces were decreased to ~ 10 µm. Secondary phases in the $Mg_{95.8}Zn_{3.6}Gd_{0.6}$ alloy near the TMAZ/SZ interface at the AS were broken up, but most particles distributed largely along lines (Fig. 4c). Figure 4d shows that the thick LPSO plates in the $Mg_{97}Cu_1Y_2$ alloy next to the TMAZ/SZ interface were also deformed and broken up, and a large amount of small lamellae appeared in the Mg matrix.

Figure 5a shows a bright-field (BF) TEM image for a region in the TMAZ of $Mg_{95.8}Zn_{3.6}Gd_{0.6}$ near the TMAZ/SZ interface, showing particles with relatively sharp corners distributing within a narrow band, which is similar to SEM observations shown in Fig. 4c. They were identified as IQCs. Interestingly, adjacent IQC particles usually exhibited similar orientations. For example, the fivefold zone axes of two neighboring IQC particles deviate from each other by only about 2.8°, as shown by inset SAED patterns in Fig. 5a. This implies that those small IQC particles should be likely from one coarse IQC particle which was broken up during FSW. Besides IQC particles as the main secondary phase, SAED analyses indicated that a small amount of W-phase particles with complex morphologies appeared in severely deformed $Mg_{95.8}Zn_{3.6}Gd_{0.6}$ within regions close to the TMAZ/SZ interface, as shown in Fig. 5b. Furthermore, coexistence of IQC and W phases with a specific orientation relationship was observed within severely deformed $Mg_{95.8}Zn_{3.6}Gd_{0.6}$ in the TMAZ, as shown in Fig. 5c, d. The $[\bar{1}13]_W$ zone axis of these W-phase particles is parallel to the fivefold of IQCs, and the $\{220\}_W$ reciprocal spots of W-phase are almost coincident with the twofold $\{442, 002\}$ reciprocal spots of IQCs, which is consistent with that in annealed samples [34, 36]. Therefore, a small amount of IQCs was transformed into W-phase in the TMAZ, besides breakup of IQCs induced by SPD during FSW.

Figure 6 shows TEM images for a region in the TMAZ of $Mg_{97}Cu_1Y_2$ near the TMAZ/SZ interface. Figure 6a shows a low-magnification BF TEM image for a thick LPSO plate, demonstrating the occurrence of plastic deformation which resulted in fracture and local bending, as indicated by white arrows. According to SAED analyses (inset in Fig. 6a), the thick plate has the 18R-LPSO structure. Diffraction spots show a characteristic of splitting, as a result of local bending of the LPSO plate. Interestingly,
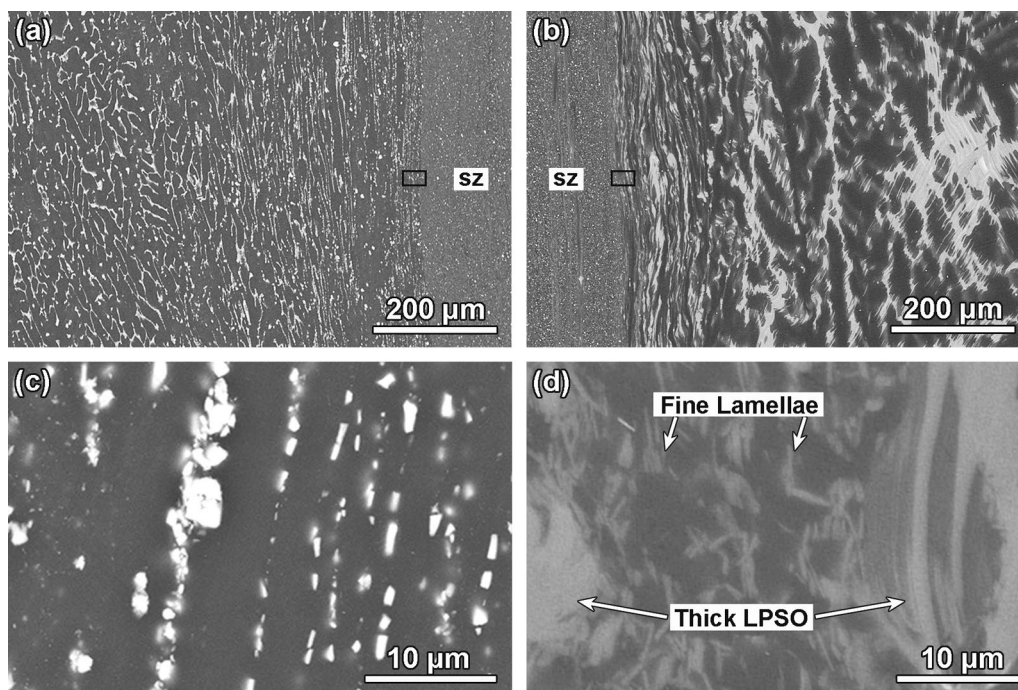

Fig. 4 a, **b** BSE-SEM micrographs for TMAZ at AS and RS, respectively. **c**, **d** Magnified images for regions indicated by black rectangles in **a**, **b**, respectively
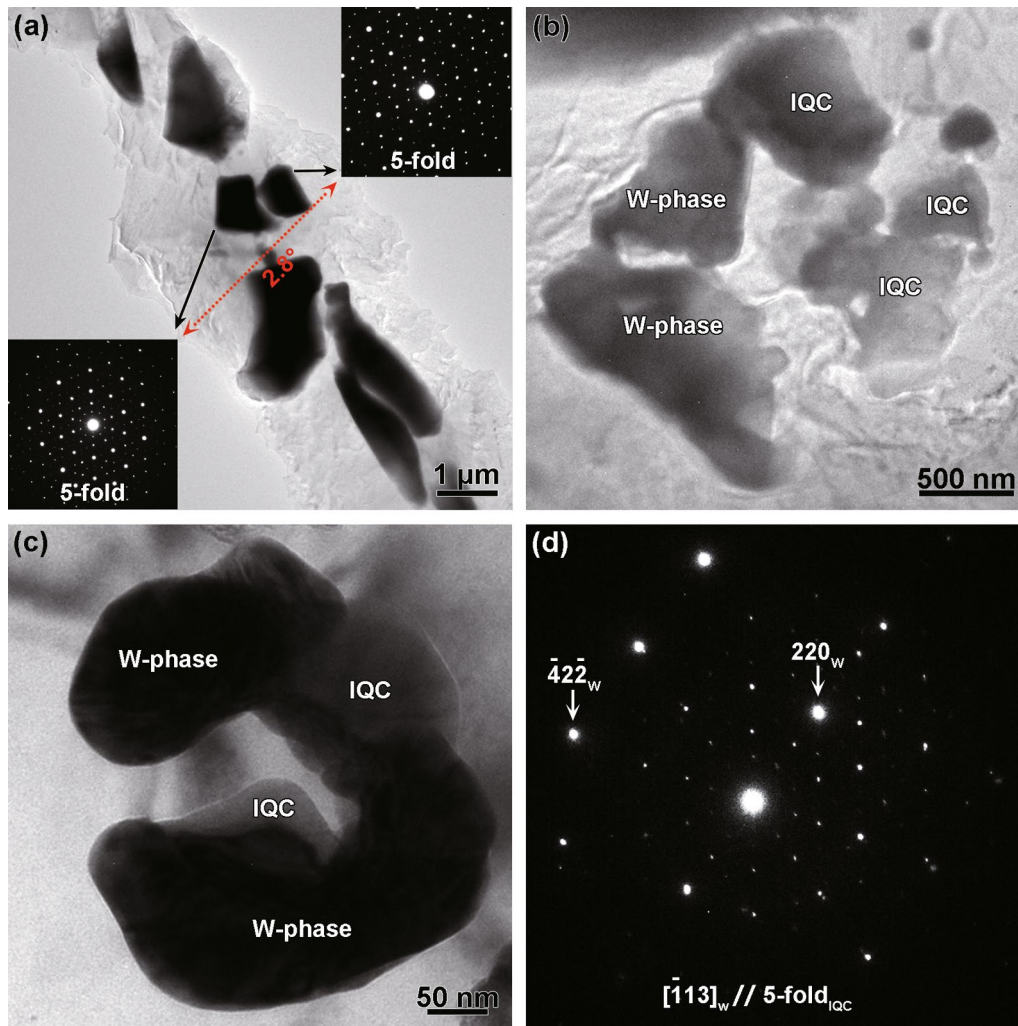
Fig. 5 Microstructure of TMAZ near the TMAZ/SZ interface at the advancing side: **a** a low-magnification image showing breakup of IQCs, inset SAED patterns for particles indicated by black arrows along the fivefold axis, **b** W-phase and IQC particles with random orientation. **c, d** A TEM image and corresponding composite SAED pattern showing IQC and W particles with a specific orientation relationship

it is found that there are usually many small lamellae distributing randomly within Mg matrix surrounding thick deformed LPSO plates, when observed at higher magnifications, as shown in Fig. 6b. SAED analyses indicated that the small lamellae indicated by white arrows were 18R-LPSO, while those indicated by black arrows were 14H-LPSO. Figure 6c, d shows high-resolution TEM images recorded along the $[11\bar{2}0]_{14H}$ zone axis for different regions. Atomic columns within the 14H-LPSO lamella could be resolved, but the adjacent α-Mg matrix did not show atomic resolution images (Fig. 6c, d), which is in contrast to the case of simultaneous atomic resolution imaging of LPSO plates and surrounding Mg matrix with a specific orientation relationship, $[11\bar{2}0]_{14H}//[11\bar{2}0]_{Mg}$ and $(0001)_{14H}//(0001)_{Mg}$, in as-cast and annealed samples [35, 37]. The loss of specific orientation relationships between small LPSO lamellae and surrounding Mg matrix was

also confirmed by SAED analyses, as shown by an inset in Fig. 6d.

3.1.3 Microstructures of SZ

A low-magnification SEM micrograph for the cross section of SZ is shown in Fig. 7a. A distinct onion-ring structure can be observed in the SZ, which is common in FSW joints [38]. Figure 7b shows a SEM micrograph for the center region of the SZ, indicating an elliptical region of about 550 μm × 240 μm. The center region is composed of α-Mg and compound particles in different sizes, as shown in a magnified BSE-SEM image in Fig. 7c. Figure 7d shows an enlarged BSE-SEM micrograph for onion rings outside the center region, indicating an alternative distribution of two kinds of layers. Secondary phases in one kind of layer are mainly granular particles, as indicated by ''I'' in Fig. 7d,
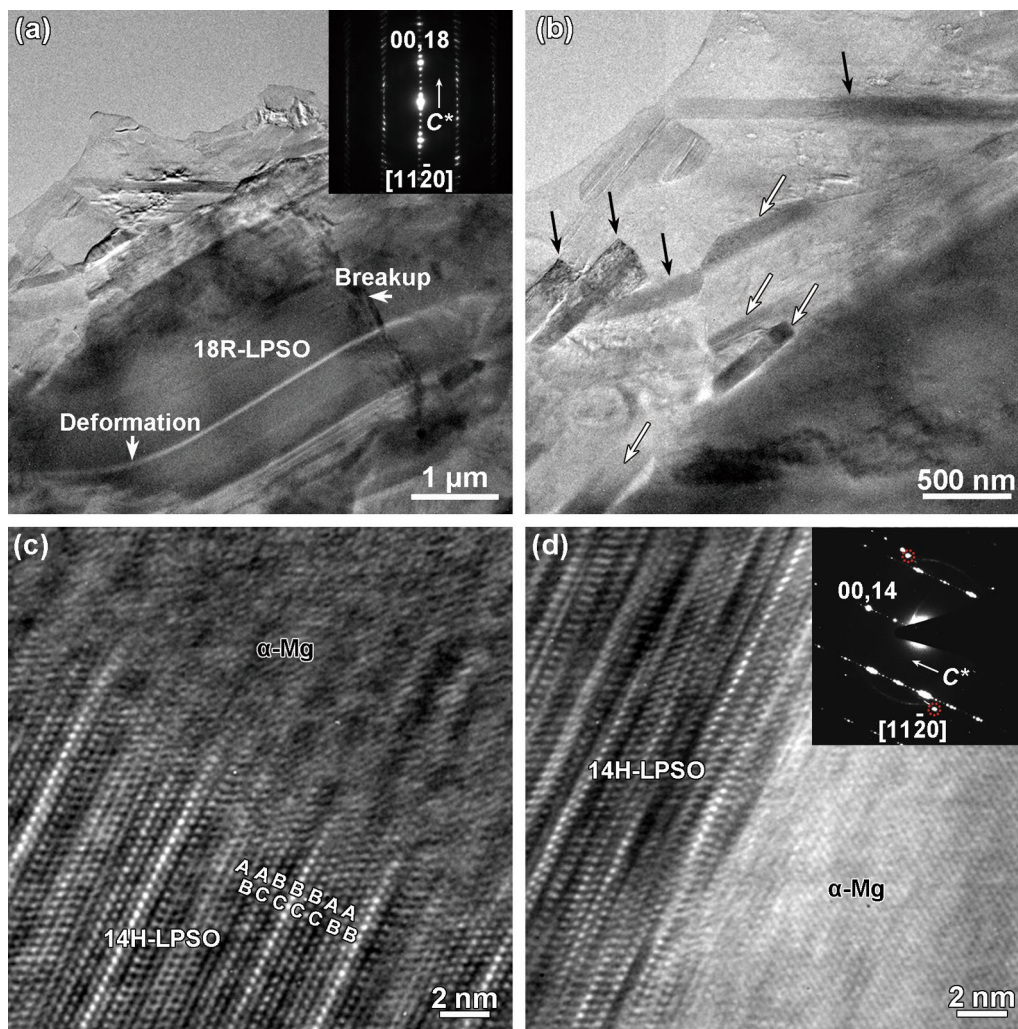
Fig. 6 Microstructure of TMAZ near the TMAZ/SZ interface at the retreating side: **a** a low-magnification image showing bending and fracture of a thick LPSO plate, and an inset SAED pattern recorded along the [$11\bar{2}0$] zone axis, **b** a magnified image showing small lamellae within Mg matrix adjacent to one thick18R-LPSO plate. **c**, **d** High-resolution TEM images for regions containing 14H-LPSO lamellae and surrounding α-Mg matrix. Inset in **d** is a corresponding composite SAED pattern recorded along the [$11\bar{2}0$] zone axis of the 14H-LPSO lamella, and diffraction spots from adjacent Mg matrix are indicated by dotted circles

which is the same as the center region. The other kind of layer contains a large number of fine lamellae of secondary phases, as indicated by ''II'' in Fig. 7d. Therefore, this result clearly shows that the SZ consists of a particle-rich center region surrounded by an onion-ring structure composed of alternative particle-rich and lamella-rich layers.

Figure 8a–c shows SEM images taken, respectively, from the center region and onion-ring regions at AS and RS of the SZ, showing morphologies and sizes of Mg grains in corresponding regions. Bands with finer and coarser grains correspond to, respectively, lamella-rich and particle-rich layers, as indicated by red dotted lines in Fig. 8b, c. Figure 8d–f shows statistical results of grain sizes in the center region, particle-rich and lamella-rich layers in the onion-ring region, respectively. Most grains in the center region

and particle-rich layers of the onion-ring region are both in a range of 1–4 μm and 0.6–1.8 μm in lamella-rich layers. Therefore, significant grain refinement was achieved in the overall SZ, compared with as-cast samples (Fig. 3).

Figure 9a, b shows low-magnification HAADF-STEM images for the particle-rich center region and the onion rings, respectively. It is interesting to note that granular particles in the center region and particle-rich layers of onion rings were mostly identified as face-centered cubic (FCC) W-phase (space group $Fm\bar{3}m$, $a = 0.683$ nm), based on SAED analyses, as shown in Fig. 9c–e. Comprehensive SAED analyses found that particles with diameters of 0.5–1 μm were mostly FCC W-phase, while a small fraction of particles 0.1–0.5 μm in diameters were IQCs, in particle-rich regions. Fine lamellae in the lamella-rich layers were
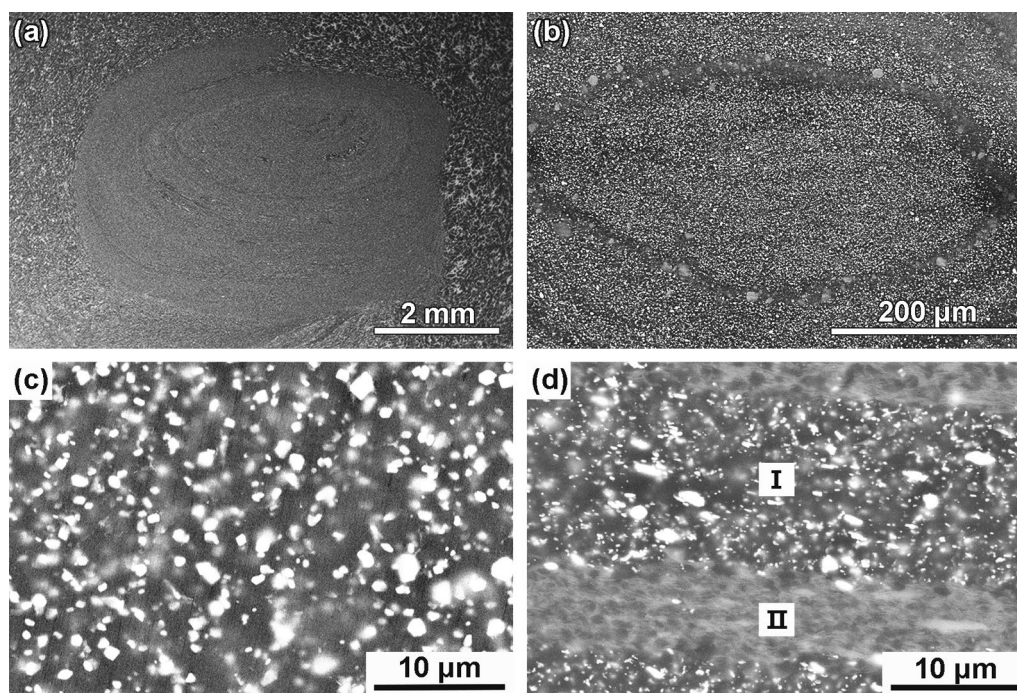
Fig. 7 **a** A low-magnification SEM micrograph of the SZ, **b** a BSE-SEM micrograph of the center region. **c, d** Magnified BSE-SEM micrographs for the center region and onion rings, respectively

identified as 14H-LPSO by SAED (Fig. 9f). The lamella-rich layers can thus be referred to as LPSO-rich layers.

Figure 10a shows a medium-magnification HAADF-STEM image showing that a large number of nanometer precipitates (5–50 nm) were formed in the Mg matrix of particle-rich regions, besides those relatively larger particles of W-phase and IQCs (Fig. 9). This is somewhat different from the presence of a small amount of fine secondary particles mainly at regions quite close to coarse IQCs at GBs in as-cast samples [6]. Figure 10b shows a typical atomic resolution HAADF-STEM image recorded along the $[0001]_{Mg}$ zone axis from a region with a nanoprecipitate, demonstrating formation of C14 hexagonal Laves $MgZn_2$ with stacking faults on basal, prismatic and pyramidal planes [39], as indicated, respectively, by white, yellow and red arrows. The orientation relationship between the $MgZn_2$ precipitate and α-Mg matrix is determined to be $[11\bar{2}0]_{MgZn2}//[0001]_{Mg}$ and $(0001)_{MgZn2}//(11\bar{2}0)_{Mg}$.

Figure 11a shows a BF TEM image showing presence of secondary particles in grain interior and at GBs in the SZ. No specific orientation relationship was observed between the α-Mg matrix and most granular particles according to SAED analyses. The two particles indicated by arrows at a GB were identified as FCC W-phase and IQC, respectively, according to SAED analyses. Those particles in the SZ (Fig. 11a) usually have smooth surfaces without sharp corners, in contrast to those fragmented IQC particles in the TMAZ (Fig. 5a), as a result of complex material flow and

heating effect in the severely deformed SZ [18]. Figure 11b shows a BF TEM image for LPSO phases in the SZ. It can be seen that small LPSO plates in the local region were not parallel with each other like those coarse LPSO plates in the as-cast material (Fig. 3b) [8], which is consistent with the SEM observation shown in Fig. 9. Most 14H-LPSO lamellae in the SZ have no specific orientation relationship with surrounding Mg matrix, which is in agreement with cases in the TMAZ shown in Fig. 6b–d.

In order to obtain chemical interaction which might occur between dissimilar layers during their complex flow and mixing, besides phase transformations mentioned above, chemical composition was evaluated by elemental mapping. Figure 12a shows a HAADF-STEM image for the onion rings with alternative distribution of particle-rich and LPSO-rich layers. Figure 12b shows EDS elemental maps for the region indicated by the white square in Fig. 12a, demonstrating that granular particles (IQC phase or W-phase) contain Cu and Y elements, in addition to Mg, Zn and Gd elements in IQCs in as-cast $Mg_{95.8}Zn_{3.6}Gd_{0.6}$ alloy. Figure 12c shows EDS mapping results obtained from the region indicated by the black square in Fig. 12a, indicating that LPSO plates contain Zn and Gd elements, besides Mg, Cu and Y elements in those LPSO plates in as-cast $Mg_{97}Cu_1Y_2$ samples. Therefore, EDS results demonstrated clearly the occurrence of long-range diffusion accompanying the SPD during FSW, which should be closely related with the generation of a high density of crystal defects, such as dislocations and GBs,
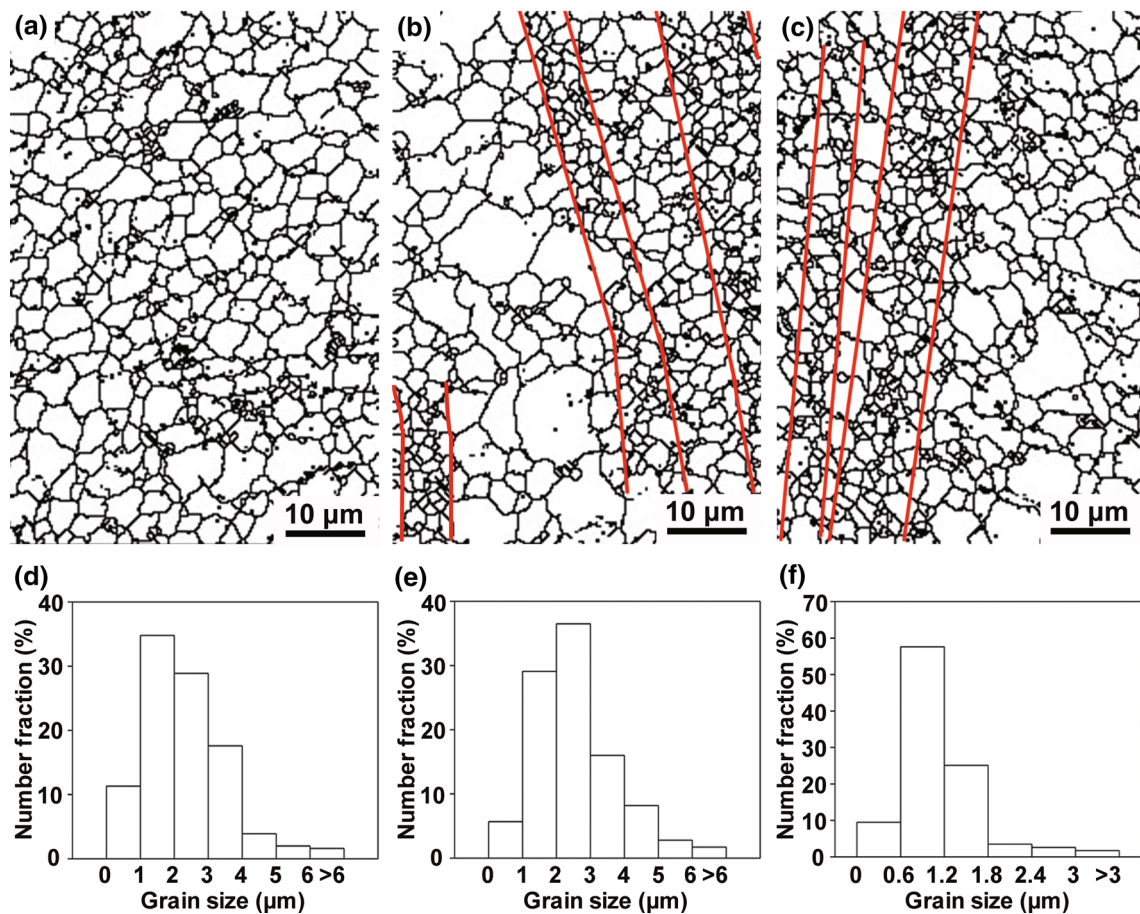
Fig. 8 SEM GB maps of **a** center region, **b** layers of onion rings at advancing side, **c** layers of onion rings at retreating side. **d–f** Statistical results of grain sizes in the center region, particle-rich and lamella-rich layers in the onion-ring region, respectively

enhancing diffusion significantly [40, 41]. The occurrence of interdiffusion between adjacent layers should benefit inter-layer metallurgical bonding principally.

3.2 Mechanical Properties

Vickers microhardnesses of coarse IQCs and LPSO plates in base materials were measured to be, respectively, 82.2 ± 3.1 Hv and 104.0 ± 3.2 Hv, higher than that of the corresponding Mg matrix of 73.7 ± 1.6 Hv (AS) and 66.7 ± 1.6 Hv (RS), respectively. Results of microhardness measurements across the dissimilar joint are summarized in Table 1. The SZ has an average microhardness of 83.9 ± 2.6 Hv which is higher than that of Mg matrix in both base materials, due to grain refinement and dispersion of fine particles of W-phase and LPSO, as well as $MgZn_2$ nanoprecipitates in the SZ, as shown in Figs. 4, 5, 7, 8, 9 and 10. The microhardness in Mg matrix of TMAZ of $Mg_{95.8}Zn_{3.6}Gd_{0.6}$ and $Mg_{97}Cu_1Y_2$ was increased to, respectively, 76.4 ± 2.3 Hv and 74.0 ± 6.6 Hv, which should be mainly attributed to strain hardening, since no obvious microstructural refinement was observed for

most regions in the TMAZ (Fig. 4a, b). Interestingly, there is a narrow region (~ 200 μm wide) within the TMAZ next to the SZ/TMAZ interfaces showing higher microhardness of 82.9 ± 6.1 Hv and 94.4 ± 14.4 Hv at AS and RS, respectively, compared with Mg matrix of other regions in the TMAZ. This should be attributed to the fact that the width of Mg grains in such regions was decreased to about 10 μm which is smaller than the diagonal of indents (~ 20 μm), and the presence of an array of secondary phase particles at each GB, as shown in Fig. 4.

Figure 13 summarizes tensile properties of the SZ and the base materials. The ultimate tensile strength and elongation to failure for the as-cast $Mg_{95.8}Zn_{3.6}Gd_{0.6}$ are 253.4 ± 4.8 MPa and $10.2\% \pm 0.4\%$, and 194.1 ± 9.7 MPa and $14.9\% \pm 0.8\%$ for as-cast $Mg_{97}Cu_1Y_2$, respectively. The dissimilar SZ exhibits improved tensile properties of $\sigma = 415.4 \pm 2.5$ MPa and $\delta = 27.8\% \pm 0.5\%$, in comparison with both base materials. This simultaneous improvement in tensile strength and ductility for the present dissimilar
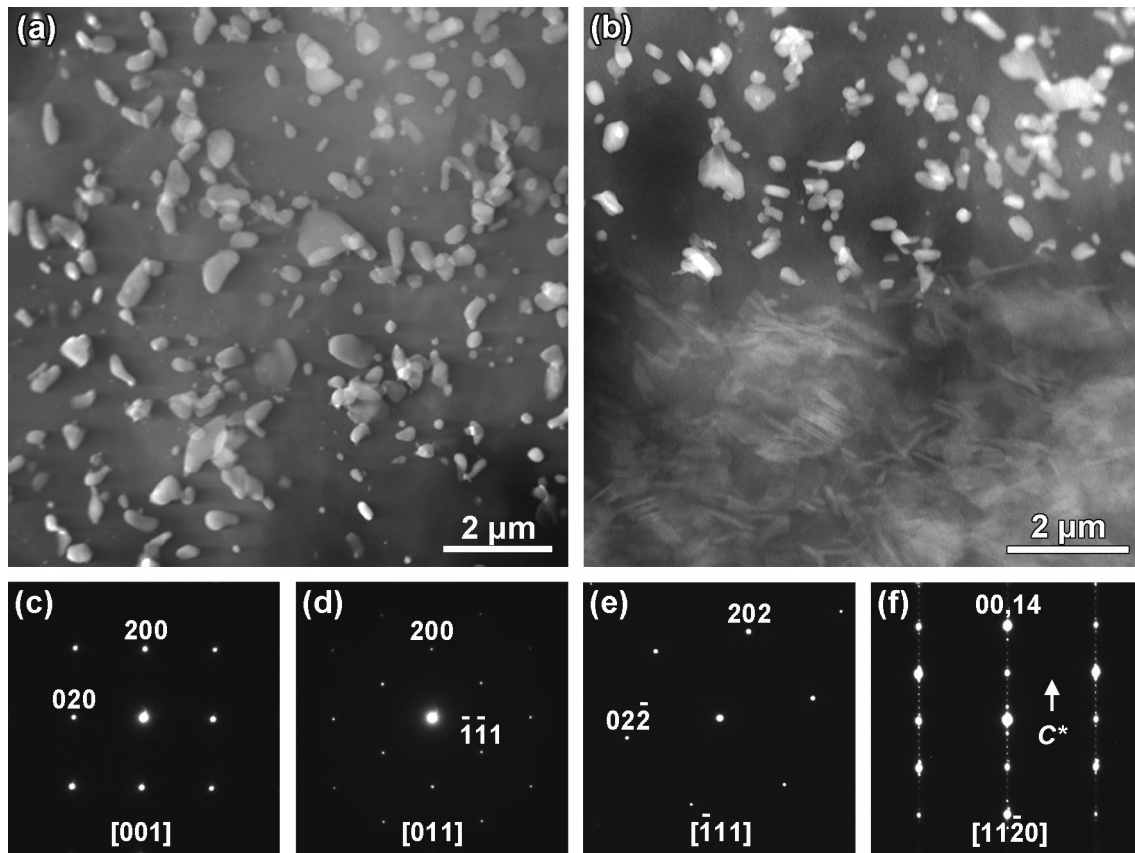
Fig. 9 Low-magnification STEM images for **a** particle-rich center region and **b** onion rings. **c–e** SAED patterns of W-phase particles along the [001], [011] and [$\bar{1}$ 11] zone axis, respectively. **f** SAED pattern of lamella phases in the lamella-rich layer along the [11 $\bar{2}$ 0] zone axis
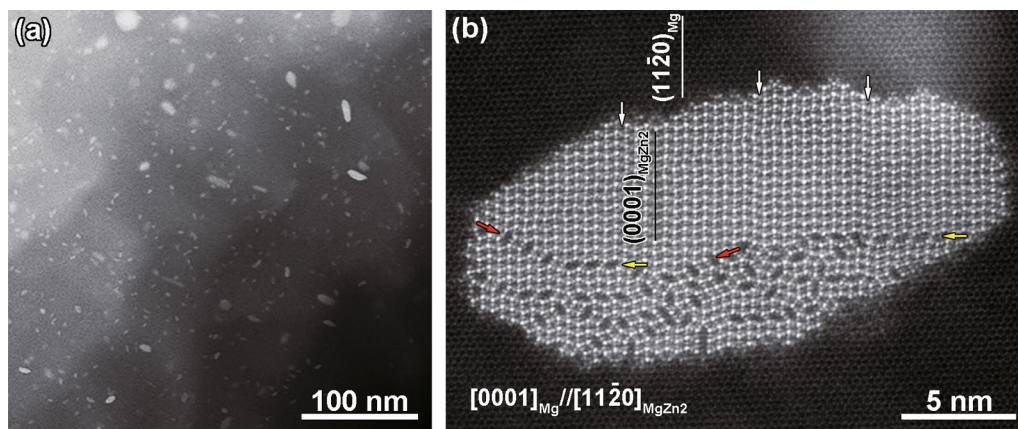

Fig. 10 **a** A low-magnification HAADF-STEM image for nanoprecipitates in Mg matrix, **b** an atomic resolution HAADF-STEM image recorded along the [0001]$_{Mg}$ zone axis for a region with a precipitate

SZ is different from the decrease in tensile strength of a Mg–Zn–Y–Zr alloy with IQCs subjected to FSW [27], and the decrease in tensile ductility of a FSPed Mg–Gd–Zn–Zr alloy with LPSO phases [25].

4 Discussion

4.1 Phase transformation

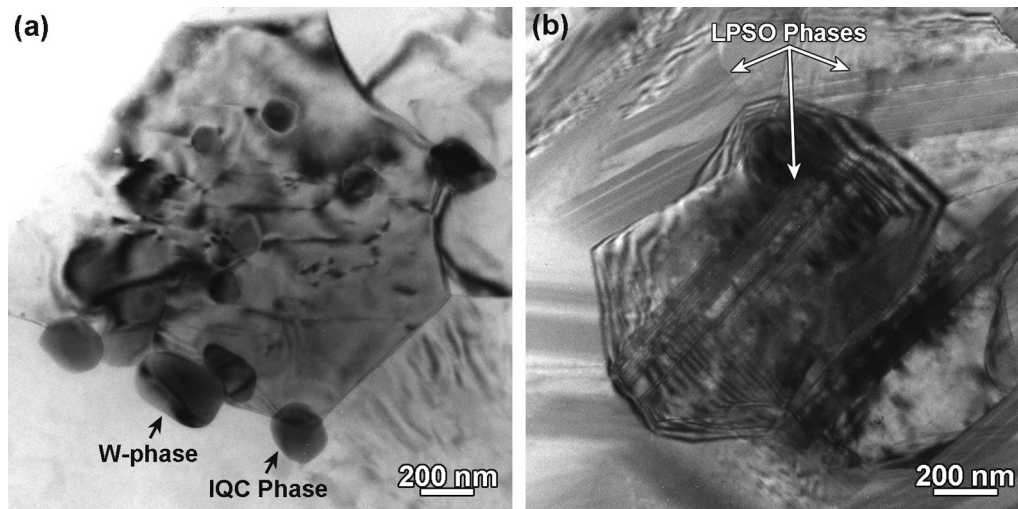Based on microstructural investigations, it can be

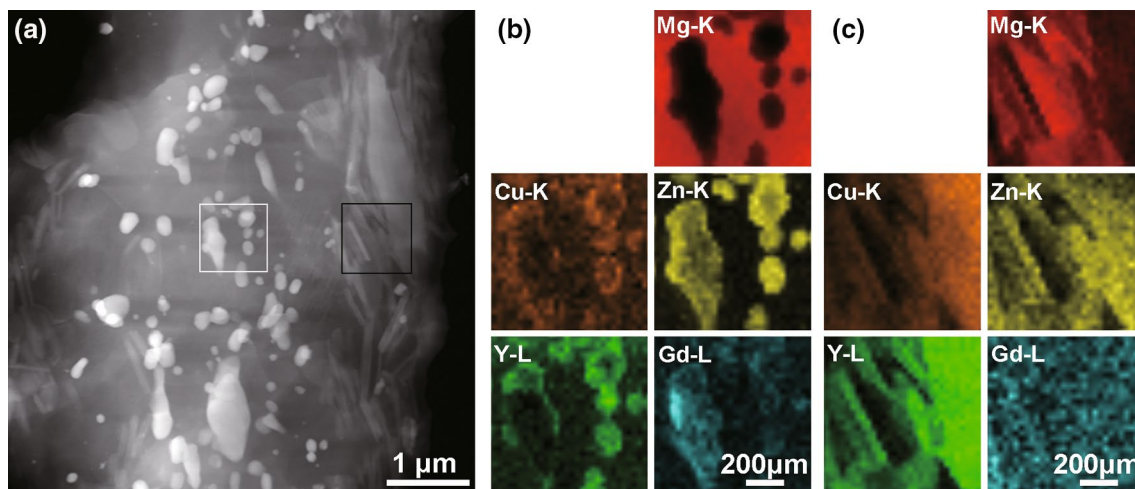**Fig. 11** TEM images for **a** granular particles, **b** LPSO lamellae in the SZ

Fig. 12 a A low-magnification STEM image for the onion-ring region, **b**, **c** EDS mappings for the white and black rectangular regions indicated in **a**

Table 1 Vickers microhardness for the SZ, severely deformed regions ~150 μm wide in the TMAZ next to the TMAZ/SZ interfaces (referred to as interface for short), Mg matrix in TMAZ and BM. Microhardness for IQC and LPSO in BM is shown in the corresponding bracket

BM	TMAZ (AS)	Interface (AS)	SZ	Interface (RS)	TMAZ (RS)	BM
73.7 ± 1.6 (82.2 ± 3.1)	76.4 ± 2.3	82.9 ± 6.1	83.9 ± 2.6	94.4 ± 14.4	74.0 ± 6.6	66.7 ± 1.6 (104.0 ± 3.2)

concluded that SPD of FSW resulted in significant grain refinement, breakup of secondary phases and their dispersive distribution. It is largely accepted that dynamic recrystallization (DRX) governs grain refinement during FSW or FSP [18, 24]. The formation of fine particle of secondary phases and their random distribution were attributed to significant breakup and dispersion effect of the threaded pin during FSW [26, 27].

An important feature in the SZ is the onion-ring structure with alternate distribution of particle-rich and LPSO-rich layers (Fig. 4d). It has been reported that this structure was formed through an ordered deposition of extruded layers that go through the threaded pin [21]. The present microstructural investigations indicated that materials in the central region should be mainly from the base material of $Mg_{95.8}Zn_{3.6}Gd_{0.6}$, since most of the secondary particles were
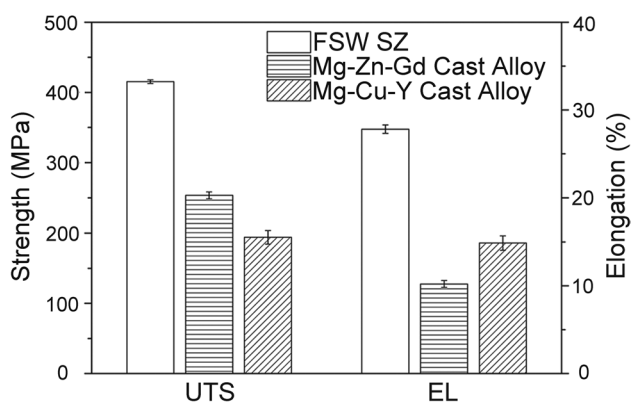
Fig. 13 Tensile properties of SZ and as-cast samples

identified to be FCC W-phase particles, while few LPSO plates were observed, as shown in Fig. 9a. In onion-ring regions of the SZ, most granular particles were also identified as FCC W-phase (Fig. 9c–e), and thin lamellae were determined to be 14H-LPSO plates (Fig. 9f). Coexistence of W-phase and IQC particles with a specific orientation relationship was observed in the TMAZ of $Mg_{95.8}Zn_{3.6}Gd_{0.6}$, besides breakup of coarse IQCs (Fig. 5), providing evidence for the occurrence of transformation from IQCs to W-phase. Thin 14H-LPSO lamellae without specific orientation relationship with the matrix Mg grains were observed close to some deformed thick 18R-LPSO plates in the TMAZ of $Mg_{97}Cu_1Y_2$ (Fig. 6). These microstructural results about the TMAZs indicate that transformation from W-phase to IQC and from 18R-LPSO to 14H-LPSO had already taken place, before dissimilar layers were mixed together during the SPD of FSW.

Liu et al. [34] carried out systematic investigations on transformation of IQC phase during heat treatment, showing that IQCs began to transform to W-phase at about 720 K in Mg–Zn–Y samples. During FSP of rare earth Mg alloys, the peak temperature in the SZ might reach up to 793 K [30], which is thus high enough to activate transformation from IQCs to W-phase. In addition, initial coarse IQC particles were broken up into smaller particles (Figs. 4, 5), which might not only introduce defects into the relevant IQC particles, but also generate more IQC/Mg interfaces for nucleation and growth of W-phase particles [34]. The generation of a high density of crystal defects, such as dislocations and GBs, can significantly enhance diffusion (Fig. 12) [40, 41], which can facilitate the diffusion-mediated growth of W-phase particles [34]. Therefore, most IQC particles were transformed into W-phase within the SZ which experienced complex flow and mixing, as well as the highest level of plastic strain and temperature increase within the whole workpieces during dissimilar FSW of the $Mg_{95.8}Zn_{3.6}Gd_{0.6}$ and $Mg_{97}Cu_1Y_2$ alloys. Since the temperature increase and

plastic strain in the TMAZ are both lower than that in the SZ, only a small amount of IQC phase transformed into W-phase in the TMAZ of $Mg_{95.8}Zn_{3.6}Gd_{0.6}$, as shown in Fig. 5.

The transformation from 18R-LPSO to 14H-LPSO in Mg alloys during heat treatments has been observed in previous studies [35, 42, 43]. Zhu et al. [42] proposed that the transformation from 18R-LPSO to 14H-LPSO involved formation of stacking faults in 18R-LPSO and cooperative gliding of Shockley partial dislocations in a $Mg_{96.7}Zn_{0.8}Y_{2.4}Zr_{0.2}$ alloy, based on observations of local atomic shuffle. Takanori et al. [43] found that 18R-LPSO in a $Mg_{97}Zn_1Y_2$ alloy transformed into 14H-LPSO completely after aging for 50 h at 773 K, and they also proposed a diffusionaldisplacive transformation mechanism. Plastic deformation of LPSO in Mg alloys has been demonstrated to be dominated by basal dislocation glide [8], and full dislocations may dissociate into partials inducing local chemical and structural modification simultaneously during plastic deformation [41], which could assist the 18R-to-14H transformation of LPSO plates through generation and glide of basal dislocations. The temperature is high enough to drive long-range diffusion of alloying elements within the SZ experiencing SPD, as shown in Fig. 12. 18R-to-14H transformation of LPSO lamellae could thus take place quickly under the combination effect of temperature increase and severe plastic deformation during FSW [42, 43]. Furthermore, it should be noted that although the temperature and plastic strain in the TMAZ are both lower than that in the SZ, it is sufficient to activate structural transformation of fine LPSO plates, besides inducing fracture of thick LPSO plates (Fig. 6).

4.2 Strengthening and Toughening Mechanisms

Grain refinement has been widely proved to be very effective in strengthening engineering alloys [44]. Moreover, grain refinement not only can impede deformation twinning which may result in mechanical anisotropy [45], but also can enhance grain rotation, GB sliding and DRX which can improve ductility of Mg alloys with micrometer grains [46]. Therefore, grain refinement to a few micrometers in the SZ should principally play a significant role in simultaneous increase in hardness, tensile strength and ductility of the SZ in the present $Mg_{95.8}Zn_{3.6}Gd_{0.6}/Mg_{97}Cu_1Y_2$ dissimilar joints (Fig. 13). In addition, fine compound particles (< 1 μm) distributing in Mg matrix (Figs. 7, 9, 10, 11, 12) can play an important role in pinning mobile dislocations and impeding dynamic recovery [47], which is also responsible for the enhanced strength of the SZ. Moreover, breakup of coarse secondary phases reduces the possibility of cracking and interfacial debonding during tensile deformation, also benefiting the ductility of the SZ [48].

However, transformation of IQCs into W-phase could impair tensile properties of Mg alloys, since W-phase/Mg

interfaces are weaker than IQC/Mg interfaces [9]. This might be one of the reasons why the tensile strength of a Mg–Zn–Y–Zr alloy was decreased to 95% of the base material due to FSW, in which a fraction of IQC particles into W-phase particles [26]. Interestingly, the tensile strength and ductility of the present dissimilar FSW joints are higher than those of both base materials $Mg_{95.8}Zn_{3.6}Gd_{0.6}$ and $Mg_{97}Cu_1Y_2$, although most IQCs were transformed into W-phase in the SZ (Fig. 9). This implies that there should be strengthening factors other than those mentioned above for the present dissimilar FSW SZ. Construction of laminated structures has been proved to be able to produce materials with high strength and good ductility in various material systems since the ancient times [49]. Therefore, the simultaneous increase in tensile strength and ductility of the present dissimilar FSW SZ should be partly attributed to the formation of an onion-ring laminated structure with alternative arrangement of layers rich in W-phase particles and LPSO lamellae, respectively, in the SZ (Fig. 7), besides microstructural refinement. Further investigations on interfaces of the laminated structure in the SZ and deformation mechanisms, as well as the effect of FSW parameters, are deserved, in order to understand the strengthening mechanisms and hence to optimize properties of FSWed dissimilar alloys with IQCs and LPSO structures.

5 Conclusions

Comprehensive microstructural investigations were carried out, in order to understand the evolution of IQCs and LPSO phases during complex material flow and mixing of $Mg_{95.8}Zn_{3.6}Gd_{0.6}$ and $Mg_{97}Cu_1Y_2$ alloys subjected to FSW. The following conclusion can be drawn:

(1) An onion-ring structure with alternative arrangement of particle-rich and LPSO-rich layers around a particle-rich core was formed in the SZ. The particle-rich and LPSO-rich layers were produced from the base materials of $Mg_{95.8}Zn_{3.6}Gd_{0.6}$ and $Mg_{97}Cu_1Y_2$, respectively.

(2) Coarse IQCs in $Mg_{95.8}Zn_{3.6}Gd_{0.6}$ were broken up and dispersed with most of them being transformed into W-phase particles, and thick 18R-LPSO plates in $Mg_{97}Cu_1Y_2$ were fragmented and transformed into small 14H-LPSO lamellae, under the combination effect of SPD and temperature increase in the SZ. Both W-phase and 14H-LPSO particles formed during the SPD of FSW have no specific orientation relationships with the Mg matrix. In addition, a high density of nanometer $MgZn_2$ precipitated in the Mg matrix of particle-rich layers. Interlayer diffusion occurred accompanying the phase transformation of strengthening phases during complex material flow and mixing of dissimilar alloys.

(3) The SZ shows an ultimate tensile strength of about 415.4 MPa and an elongation to failure of about 27.8% which are higher than both as-cast materials. Simultaneous increase in tensile strength and ductility should be attributed to the formation of a laminated structure consisting of refined Mg grains and strengthening particles.

References

[1] B.L. Mordike, T. Ebert, Mater. Sci. Eng. A **302**, 37 (2001)

[2] L.Z. Liu, X.H. Chen, J.F. Wang, L.Y. Qiao, S.Y. Gao, K. Song, C.Y. Zhao, X.F. Liu, D. Zhao, F.S. Pan, J. Mater. Sci. Technol. **35**, 1074 (2019)

[3] M.S. Song, R.C. Zeng, Y.F. Ding, R.W. Li, M. Easton, I. Cole, N. Birbilis, X.B. Chen, J. Mater. Sci. Technol. **35**, 535 (2019)

[4] J.F. Wang, H.B. Zhou, L.G. Wang, S.J. Zhu, S.K. Guan, J. Mater. Sci. Technol. **35**, 211 (2019)

[5] D.H. Bae, S.H. Kim, D.H. Kim, W.T. Kim, Acta Mater. **50**, 2343 (2002)

[6] L.F. Zhang, S.Y. Ma, W.Z. Wang, Z.Q. Yang, H.Q. Ye, J. Mater. Sci. Technol. **35**, 2058 (2019)

[7] J.F. Wang, P.F. Song, S. Huang, F.S. Pan, Mater. Sci. Eng. A **563**, 36 (2013)

[8] X.H. Shao, Z.Q. Yang, X.L. Ma, Acta Mater. **58**, 4760 (2010)

[9] A. Singh, H. Somekawa, T. Mukai, Mater. Sci. Eng. A **528**, 6647 (2011)

[10] Y. Kawamura, T. Kasahara, S. Izumi, M. Yamasaki, Scr. Mater. **55**, 453 (2006)

[11] K. Liu, J. Meng, J. Alloys Compd. **509**, 3299 (2011)

[12] W. Rong, Y. Zhang, Y.J. Wu, Y.L. Chen, T. Tang, L.M. Peng, D.Y. Li, Mater. Charact. **131**, 380 (2017)

[13] R.Z. Valiev, I.V. Alexandrov, Y.T. Zhu, T.C. Lowe, J. Mater. Res. **17**, 5 (2002)

[14] Z.Q. Yang, U. Welzel, Mater. Lett. **59**, 3406 (2005)

[15] T.C. Lowe, R.Z. Valiev, JOM **52**, 27 (2000)

[16] N.N. Liang, Y.H. Zhao, Y. Li, T. Topping, Y.T. Zhu, R.Z. Valiev, E.J. Lavernia, J. Mater. Sci. **53**, 13173 (2018)

[17] L.L. Tang, Y.H. Zhao, R.K. Islamgaliev, R.Z. Valiev, Y.T. Zhu, J. Alloys Compd. **721**, 577 (2017)

[18] R.S. Mishra, Z.Y. Ma, Mater. Sci. Eng. R **50**, 1 (2005)

[19] S. Mironov, Y.S. Sato, H. Kokawa, J. Mater. Sci. Technol. **34**, 58 (2018)

[20] X.H. Zeng, P. Xue, L.H. Wu, D.R. Ni, B.L. Xiao, K.S. Wang, Z.Y. Ma, J. Mater. Sci. Technol. **35**, 972 (2019)

[21] D. Liu, H. Nishio, K. Nakata, Mater. Des. **32**, 4818 (2011)

[22] D.J. Liu, R.L. Xin, X. Zheng, Z. Zhou, Q. Liu, Mater. Sci. Eng. A **561**, 419 (2013)

[23] A.C. Somasekharan, L.E. Murr, Mater. Charact. **52**, 49 (2004)

[24] Z.Y. Ma, Q. Shang, D.R. Ni, B.L. Xiao, Acta Metall. Sin. **54**, 1597 (2018). **(in Chinese)**

[25] X.W. Li, F.Y. Zheng, Y.J. Wu, L.M. Peng, Y. Zhang, D.L. Lin, W.J. Ding, Mater. Lett. **113**, 206 (2013)

[26] Y.B. Wang, Y.X. Huang, X.C. Meng, L. Wan, J.C. Feng, J. Alloys Compd. **696**, 875 (2017)

[27] G.M. Xie, Z.Y. Ma, L. Geng, R.S. Chen, Mater. Sci. Eng. A **471**, 63 (2007)

[28] Q. Yang, B.L. Xiao, D. Wang, M.Y. Zheng, Z.Y. Ma, Mater. Sci. Eng. A **626**, 275 (2015)

[29] Q. Yang, B.L. Xiao, D. Wang, M.Y. Zheng, K. Wu, Z.Y. Ma, J. Alloys Compd. **581**, 585 (2013)

[30] J.Y. Han, J. Chen, L.M. Peng, F.Y. Zheng, W. Rong, Y.J. Wu, W.J. Ding, Mater. Des. **94**, 186 (2016)

[31] C. Luo, X. Li, D. Song, N. Zhou, Y. Li, W. Qi, Mater. Sci. Eng. A **664**, 103 (2016)

[32] C.I. Chang, C.J. Lee, J.C. Huang, Scr. Mater. **51**, 509 (2004)

[33] W. Woo, H. Choo, D.W. Brown, P.K. Liaw, Z. Feng, Scr. Mater. **54**, 1859 (2006)

[34] J.F. Liu, Z.Q. Yang, H.Q. Ye, J. Alloys Compd. **621**, 179 (2015)

[35] T. Itoi, T. Seimiya, Y. Kawamura, M. Hirohashi, Scr. Mater. **51**, 107 (2004)

[36] A. Singh, M. Watanabe, A. Kato, A.P. Tsai, Mater. Sci. Eng. A **397**, 22 (2005)

[37] Y.M. Zhu, A.J. Morton, J.F. Nie, Acta Mater. **58**, 2936 (2010)

[38] M. Guerra, C. Schmidt, J.C. McClure, L.E. Murr, A.C. Nunes, Mater. Charact. **49**, 95 (2002)

[39] H.Q. Ye, D.N. Wang, K.H. Kuo, Philos. Mag. A **51**, 839 (1985)

[40] M. Legros, G. Dehm, E. Arzt, T.J. Balk, Science **319**, 1646 (2008)

[41] Z.Q. Yang, W.W. Hu, L.F. Zhang, H.Q. Ye, Phys. Rev. Mater. **3**, 033602 (2019)

[42] Y.M. Zhu, A.J. Morton, J.F. Nie, Acta Mater. **60**, 6562 (2012)

[43] T. Kiguchi, Y. Ninomiya, K. Shimmi, Mater. Trans. **54**, 668 (2013)

[44] E.O. Hall, Proc. Phys. Soc. London Sect. B **64**, 747 (1951)

[45] M.R. Barnett, Z. Keshavarz, A.G. Beer, D. Atwell, Acta Mater. **52**, 5093 (2004)

[46] Z.R. Zeng, J.F. Nie, S.W. Xu, C.H.J. Davies, N. Birbilis, Nat. Commun. **8**, 972 (2017)

[47] E. Nambach, *Particle Strengthening of Metals and Alloys* (Wiley, Weinheim, 1997)

[48] W. Yuan, S.K. Panigrahi, R.S. Mishra, Metall. Mater. Trans. A **44**, 3675 (2013)

[49] D.R. Lesuer, C.K. Syn, O.D. Sherby, J. Wadsworth, J.J. Lewandowski, W.H. Hunt, Int. Mater. Rev. **41**, 169 (1996)